Tectonophysics 757 (2019) 140–152

Contents lists available at ScienceDirect

Tectonophysics

journal homepage: www.elsevier.com/locate/tecto

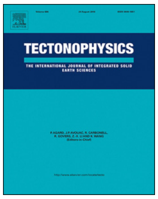

Slip perturbation during fault reactivation by a fluid injection

Maria Kakurina[a,*], Yves Guglielmi[b], Christophe Nussbaum[c], Benoît Valley[a]

[a] University of Neuchâtel, CHYN, Neuchâtel, Switzerland
[b] Lawrence Berkeley National Laboratory, Berkeley, CA, United States
[c] Swisstopo, Wabern, Switzerland

ARTICLE INFO

Keywords:
Geomechanics
Stress inversion
Slip perturbation
Wallace-Bott
Eshelby
3DEC

ABSTRACT

Slip orientation inferred from fault striae or focal mechanism datasets is commonly used in stress inversion methods based on the Wallace-Bott hypothesis. The hypothesis postulates that slip on a fault plane is collinear with the orientation of the resolved shear stress. It is valid for a single planar fault subjected to a homogeneous far-field stress. However, the experimental displacement data from an induced fault reactivation experiment, conducted in the Mont Terri rock laboratory, Switzerland, indicated multiple triggered slip orientations, thereby preventing application of the above inversion method. We present numerical and analytical results of slip on a reactivated fracture with a non-uniform fluid pressure distribution. Using these models, we evaluate the reasons for the inconsistency of our observations and the traditional Wallace-Bott hypothesis and test the physical effects of various parameters on fault slip. In the fully coupled hydromechanical numerical model (three-dimensional distinct element method), fluid pressure at a point on the fault surface is increased stepwise (assumed planar and singular) until shear reactivation of the fault is induced. We studied two different models with high and low fault plane stiffness to represent hard and soft rock masses, respectively. The model shows that high fault stiffness preserves the planarity of the fault plane, while low fault stiffness permits dilation and morphological changes of the fracture related to fluid pressure diffusion. The highest slip perturbation was observed in the low stiffness model due to the change of the fracture shape, controlled by the non-uniform pressure distribution. The Eshelby analytical solution confirmed that the more the fracture is dilated, the more the corresponding resolved shear stress is perturbed. Additionally, when compared to dilation and fault aperture, the friction angle has the most influence on the angular difference between geomechanical slip vectors and resolved shear stress.

1. Introduction

Stress inversion methods have been developed since the middle of the last century in order to estimate the in-situ stress state using focal mechanisms from earthquakes or fault slip deduced from slickenside measurements on fault planes. Generally, these inversion methods are based on the Wallace (1951) and Bott (1959) hypotheses (referred later as WB hypothesis), stating that the slip on the fault plane occurs in the direction of the maximum resolved shear traction. In 1959, Bott demonstrated that the slip direction on reactivated plane depends on the principal stress orientation, the stress ratio and the orientation of the fault plane. In addition, the WB hypothesis is based on a number of assumptions: (i) faults are planar, (ii) intact rock blocks are unbreakable, (iii) stress state is uniform, (iv) slip movements are caused by the same stress tensor, (v) neither block rotation nor stress perturbation occur along the faults, and (vi) slip movements on each fault are independent of each other.

The WB hypothesis is used to predict the kinematics of newly formed faults (Anderson, 1951; Wallace, 1951) and to estimate the potential for reactivation of natural preexisting faults planes under given regional stress states (Bott, 1959). Different methods and algorithms to reconstruct the paleostress states were developed by many authors (Angelier, 1990, 1979, 1975; Arthaud, 1969; Blenkinsop et al., 2006; Carey, 1976; Carey and Brunier, 1974; Célérier et al., 2012; Delvaux and Sperner, 2003; Etchecopar et al., 1981; Gephart and Forsyth, 1984; Hansen, 2013; Lejri et al., 2017; Lisle, 1998, 1992; Maerten et al., 2016; Reches, 1987; Yamaji, 2000). Most of these methods rely on the WB hypothesis and are applied in numerous regional studies (Angelier et al., 1985; Barrier and Angelier, 1986; Bergerat, 1987; Lacombe et al., 1990; Le Pichon et al., 1988; Letouzey, 1986; Liesa and Simón, 2009; Mattauer and Mercier, 1980; Mercier et al., 1989; Vandycke et al., 1991; Zoback et al., 1981).

However, it is legitimate to question the validity and expect limitations of the WB hypothesis for the stress estimation methods since

---

* Corresponding author.
E-mail address: maria.kakurina@unine.ch (M. Kakurina).

https://doi.org/10.1016/j.tecto.2019.01.017
Received 8 November 2018; Received in revised form 14 January 2019; Accepted 17 January 2019

many of the underlying assumptions are not honored in real field situations. Field observations of geometrical complexity of fault surfaces and fault networks (Jaeggi et al., 2017; Nussbaum et al., 2011; Wallace and Morris, 1986; Wibberley and Shipton, 2010), evidences of local stress perturbations from observed microstructures (Hancock, 1985; Laurich et al., 2014; Petit, 1987; Soliva et al., 2010), curved lineations on the local shear planes (Twiss and Gefell, 1990) imply that the mechanical problems of stress inversions are overly simplified and seem to disagree with the Wallace-Bott (WB) assumptions.

Numerical investigations of the WB assumptions, examined by Dupin et al. (1993), Kaven et al. (2011), Maerten (2000), Nieto-Samaniego and Alaniz-Alvarez (1997), Pascal (2002), Pollard et al. (1993) demonstrated that the slip direction can be strongly influenced by the mechanical interactions between closely spaced faults within the same tectonic stress regime. The mechanical interactions are partly attributed to elastic deformations that cause local stress perturbations acting on one fault plane when induced by slip on another fault plane. Indeed, in the vicinity of fault intersections, the slip direction can deviate up to 50° from the direction of resolved shear stress (Maerten, 2000). The mechanical interactions are accompanied by strain hardening behavior characterized by an increase in the fault surface roughness and by changes in deformation mode from a simple frictional sliding to a combination of sliding, dilation and formation of new fractures. Nieto-Samaniego and Alaniz-Alvarez (1997) demonstrated that those interactions affect the slip direction and, therefore, may invalidate the WB hypothesis. If fault spacing is large enough to prevent these mechanical interactions, the slip tends to follow the theoretical WB predictions.

According to the WB hypothesis, for non-planar faults, such as highly curved faults, corrugated faults, lineated portions of stylolitic surfaces, and flexural slip folds, the directions of resolved shear stress in general give a set of slip directions of rigid fault blocks, which is generally kinematically questionable (Lisle, 2013). For example, Lisle (2013) demonstrated that the anisotropy of the shear strength arising from simple fault plane topography can lead to significant angular differences between the directions of resolved maximum stress and the slip direction. Potential slip for a corrugated fault plane is oblique to the maximum resolved shear stress direction. The author also showed that the magnitudes of the high resolved shear stress (90% of the maximum values) are defined within tolerance of ± 26° of the slip direction implying that in practice a high variability around the theoretical maximum shear stress direction is expected.

More recently, Lejri et al. (2015) examined the effect of all possible Andersonian stress regimes, half space effect, fault fluid pressure, sliding friction, Poisson's ratio and various idealized fault geometries in relation to the validity of the WB assumptions. They confirmed that high angular differences (later referred as misfit angle) exist between geomechanical slip vectors and resolved shear stress under specific fault configurations such as intersecting faults or highly corrugated fault surfaces, invalidating the WB assumptions. These effects are slightly reduced when faults touch the traction free surface of the Earth where no confinement is applied. The propensity for a fault to slip at the surface is increased and slip gradients are greater than on an isolated fault at depth. According to Lejri et al. (2015), the increase of the fault friction globally lowers slip magnitude, hence mechanical interaction, and reduces the misfit angle between the slip direction and resolved shear stress. The friction effects were also investigated by Pascal (2002), who concluded that the sliding friction reduces slip perturbation and validates the WB assumptions. The Poisson's ratio has a very small effect on the misfit angles (Lejri et al., 2015).

Uniform fluid pressure inside the intersecting fault planes affects the resulting slip orientations (Lejri et al., 2015; Maerten et al., 2018). Greater fluid pressure leads to higher misfit angles (Lejri et al., 2015). This is related to the fact, that fluid pressure reduces the effective normal stress on a fault plane and thus may affect both the slip magnitude and slip vector orientation, violating the WB hypothesis. In addition, uniform fluid pressure increase in an intersecting fault situation will generate stress perturbations due to the resulting elastic deformation of the surrounding rock mass that can also explain deviation from the WB hypothesis.

Pore pressure increased by fluid injection in the vicinity of the injection borehole propagates and decays in the amplitude away from the borehole, governed by hydraulic diffusion (Shapiro et al., 2003). This is another important effect to consider when injecting in a fracture or fault is that pressure diffusion is progressive leading to a non-homogenous pressure field. Such pressure diffusion effects are known to eventually induce seismicity (i.e. fracture slips) in the surrounding rock mass (Ellsworth, 2013; Evans et al., 2012; Guglielmi et al., 2008; McGarr, 2014; Shapiro et al., 1999; Shapiro and Dinske, 2009; Zoback and Harjes, 1997). The question is whether slip under a non-uniform pressure field obeys or disobeys the WB hypothesis? Taking an example from the Geysers geothermal field, Martínez-Garzón et al. (2016) observed that slip deviation occurs on faults during periods of high injection rates close to the injection wells. However in the Basel Fluid-Injection Experiment the misfit between expected slip vectors and slip vectors deduced from the focal mechanisms was < 15 degrees and > 80% of the slip vectors were consistent with those expected under the estimated uniform stress pattern (Terakawa et al., 2012).

The consequences of a non-uniform pressure field are a non-uniform fracture opening and shear. During fluid injection, a fracture opens progressively from the borehole to the fracture tip. Stress transfers are associated with these non-uniform deformation fields leading to stress perturbations that could explain violation of the WB hypothesis (Cornet and Julien, 1989; Roche et al., 2018). With time pressure diffusion tends to equilibrate the pressure distribution leading to a more uniform fracture shape and thus at such a stage it is expected that the WB hypothesis would be valid again.

In this paper, we focus on the evaluation of the theoretical bases related to the WB hypothesis in the context of stress inversion of the slip data obtained during fault reactivation by a fluid injection. The slip data is measured following the step-rate injection method for fracture in situ properties (SIMFIP) developed by Guglielmi and Cappa (2013). Compared to a standard double packer system, in addition to flowrate and pressure monitoring the SIMFIP probe measures the three-dimensional (3D) displacement in the injection chamber. The direct in situ measurement of the 3D displacement corresponding to slip on reactivated faults allows estimation of the principal stress orientations and relative magnitudes by solving the inverse stress problem.

The SIMFIP probe was used to conduct the Fault Slip (FS) experiment of fault reactivation in shale rocks at the Mont Terri rock laboratory (Guglielmi, 2016; Guglielmi et al., 2017). The experiment focusses on understanding the conditions of fault stability and activation, as well as on evolution of the coupling between fault slip, pore pressure and fluid migration in shales. One of the main goals of the FS experiment is to develop a protocol of estimating the in situ stress using the additional displacement data information. The FS experiment consists of a sequence of pressure-controlled fluid injections into 2.4 m long intervals within the main tectonic zone of the Mont Terri rock laboratory, called the Main Fault, to reactivate the fault planes and to induce fault slip, which can be used to solve the stress inversion problem (Fig. 1a). The orientations (dip direction/dip angle convention is used in this paper) of the two boundary planes of the Main Fault vary with dip direction ranging from 140° to 165° and the dip angle – from 40° to 65°(Guglielmi et al., 2017). In total, there were five injection tests performed. Here, we investigate the results of the test conducted above the Main Fault at the depth of 40.6 m below the laboratory floor (−300 m.a.s.l.). The pressure and flowrate time variations conducted at the test are shown in Fig. 1b. The initial pressure steps are achieved by small volume injections (insignificant flowrate). When the pressure reaches 5.3 ± 0.1 MPa a significant flow rate is required to maintain the pressure which indicates fault opening. Deformation is measured during this pressure/flow history. Deformation occurs even during

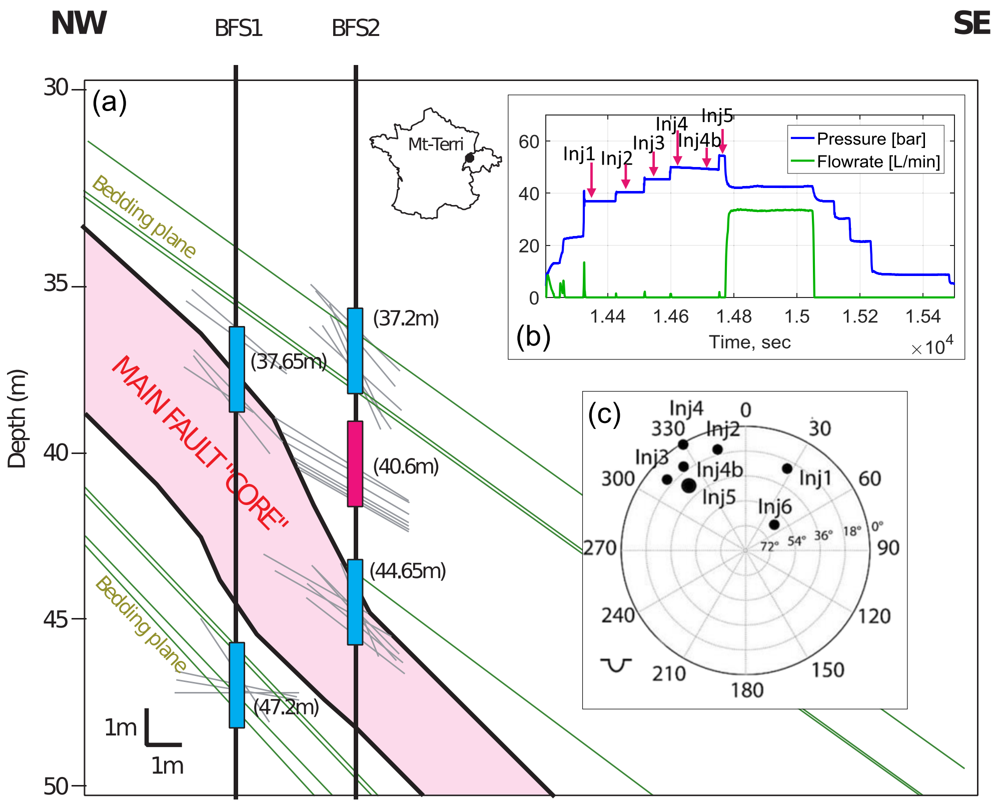

Fig. 1. (a) Simplified cross-section of the structural setting of the FS experiment (modified from Guglielmi, 2016). The locations of the test intervals are figured by the blue and pink (investigated) rectangles. (b) Pressure and injected flowrate variations monitored at the injected interval of 40.6 m depth. (c) Stereographic projection of the plastic displacement vectors picked at constant pressure, shown by pink arrows on (b). (For interpretation of the references to color in this figure legend, the reader is referred to the web version of this article.)

constant pressure in the injection chamber even with insignificant flowrate prior to fault opening pressure and we interpret this as an indication of fault rupture – fault slip. The orientations of the slip vectors are shown in Fig. 1c. It is demonstrated that slip orientation rotates in a counterclockwise direction from 029°/20° at the injection 1 to the direction of 345°/16° at the injection 2, then to the direction of 313°/17° at the injection 3. Afterwards the slip vector rotates slightly clockwise to the direction of 330°/0° at the injection 4 and then in a counterclockwise direction again at the injection 4b and 5, having the directions of 325°/17° and 320°/40°, respectively. The vector at the injection 6 has an orientation of 050°/60°, which does not follow the rotation tendency discussed above, however, this vector was measured after the fault opening, and therefore additional processes can influence its orientation. The difference in slip orientation at each pressure step does not permit a stress inversion to be carried out because the WB assumption of the stress homogeneity is not satisfied. We expect that the cause of slip deviation is in the non-uniform pressure distribution and altered fracture aperture. To investigate these complex interactions between pore pressure distribution inside the fracture and slip orientation, we built a numerical model that includes pressure diffusion and fluid flow along the fracture coupled with fracture deformation, using the three-dimensional distinct element code 3DEC (Itasca Consulting Group, 2007). We estimate the role of changes in fracture shape during fluid injection on stress perturbations using the analytical solution of stress perturbation around an ellipsoidal fracture provided by Eshelby (1957). This analytical solution helps in understanding of how the changes in fracture shape during fluid injection can affect the orientations of the slip vectors without considering the complete hydromechanical coupling. For both numerical and analytical methods, two particular models are presented here, with a high and a low fracture stiffness to emulate a fault within more competent (carbonates) and less competent (shales) rocks, respectively. The stiffness will determine the opening of the fracture affecting its shape and is thus expected to be a controlling parameter on slip direction perturbations.

In addition to the fracture stiffness coefficients, a multi-parametric study including (i) friction angles, (ii) dilation angles, and (iii) aperture was performed to understand the effect of each parameter on the misfit angle between the simulated slip vectors affected by the pressure non-uniform distribution and the resolved shear stress direction relevant in the WB hypothesis.

2. Theoretical background

2.1. Orientation of the resolved shear stress (Wallace-Bott hypothesis)

The rake of the displacement that is consistent with the resolved shear stress according to the Wallace-Bott hypothesis can be computed by methods proposed by Bott (1959) and Jaeger et al. (2009). The normal and shear traction components on the plane P with a dip angle θ and a dip direction of λ can be expressed in a local Cartesian coordinate system (x', y', z') with x' down dip, y' horizontal and z' normal to P (Fig. 2). The dip angle and dip direction are defined relatively to the far field principal stress coordinate system x-axis (σ_1), y-axis (σ_2) and z-axis (σ_3). The normal (σ) and shear components ($\tau_{z'y'}$, $\tau_{z'x'}$) on the plane P are given by:

$$\sigma = (\sigma_1 \cos^2\lambda + \sigma_2 \sin^2\lambda)\sin^2\theta + \sigma_3 \cos^2\theta \tag{1}$$

$$\tau_{z'y'} = -\frac{1}{2}(\sigma_1 - \sigma_2)\sin\theta\sin 2\lambda \tag{2}$$

$$\tau_{z'x'} = \frac{1}{2}(\sigma_1 \cos^2\lambda + \sigma_2 \sin^2\lambda - \sigma_3)\sin 2\theta \tag{3}$$

The rake α of the maximum shear traction on the plane is obtained by combining Eqs. (2) and (3) and is given by:

$$\alpha = \arctan\frac{\tau_{x'z'}}{\tau_{y'z'}} = \arctan\frac{2(\cos^2\lambda + \Phi\sin^2\lambda)\cos\theta}{(1-\Phi)\sin 2\lambda} \tag{4}$$

where $\Phi = (\sigma_2 - \sigma_3)/(\sigma_1 - \sigma_3)$ is refered as the stress ratio. In Eq. (4),

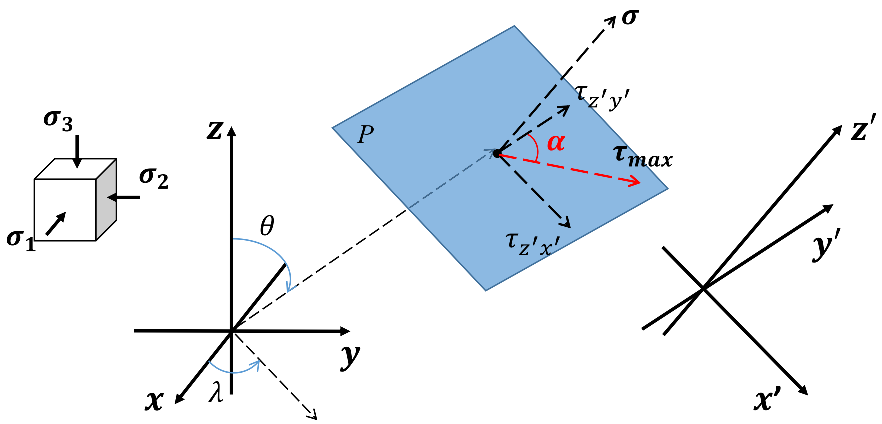

Fig. 2. Principal stress coordinate system (x, y, z) and local Cartesian coordinate system (x', y', z') with the slip vector α of the maximum resolved shear stress. The plane P (blue rectangle) is expressed in a local coordinate system with dip angle θ and dip direction λ relatively to the principal stress coordinate system. The shear components $\tau_{z'y'}$ and $\tau_{z'x'}$ are in the directions of strike and dip of the plane P, respectively. (For interpretation of the references to color in this figure legend, the reader is referred to the web version of this article.)

the direction of the maximum resolved shear stress (τ_{max}) on a plane depends only on the plane's orientation with respect to the principal stress orientations and their magnitude ratio Φ. In our study, we used the implementation of these equations in Faultkin software (Allmendinger et al., 2011; Marrett and Allmendinger, 1990) to compute the rake of the maximum resolved shear traction.

2.2. Problem statement and conceptual model

When fluid is injected into a fault zone (we will initially make the simplification that the fault is represented as a single planar fracture), it activates a series of thermo-hydromechanical processes that will affect the rock mass condition and the fracture shape (Fig. 3).

We assume isothermal fluid injection and thus focus only on the following hydromechanical processes. When fluid is injected into the fault, the fluid will diffuse preferentially in the fault itself and the diffusion will be controlled by the hydraulic aperture of the fault. This will first induce an elastic response of the fracture and the rock mass surrounding it. The pressure increase in the fault plane will generate an elastic opening of the plane with a normal displacement component (ΔU_n) that in turn will modify the hydraulic aperture and involve a non-linear diffusion process. The opening of the fault plane will be accommodated by the deformation of the surrounding rock inducing elastic stress changes $\Delta\sigma_e$ around the injection point. The deformation and the stress changes will be controlled by the stiffness properties of the fault plane and of the surrounding rock as well as by the non-homogeneous pressure distribution around the injection location. Such a complex fully coupled hydromechanical process is likely to induce some local rotation of the principal stresses, resulting eventually in the "violation" of the WB hypothesis.

In addition, the pressure increase in the fault plane will reduce the effective normal stress. If sufficient shear traction is resolved on the fault plane, this will eventually drive the plane to shear failure and be associated with slip. In contrast to the elastic response described above, the slip associated with shear failure is typically not reversible and we will refer to it as plastic deformation. The initiation of slip is controlled on one hand by the frictional properties of the plane (no cohesion is assumed) and on the other hand by the shear traction τ acting on the plane that depends on the local stress state (Mohr-Coulomb criterion). The frictional properties are assumed to be invariant, although modification of the frictional properties due to wetting and/or lubrication or other rock/fluid interactions is possible. Associated with fault slip, stress will be redistributed with a relaxation of the shear stress on the fault plane and a concentration of stresses near the fault tip ($\Delta\sigma_p$). Mechanical dilation of the fault plane can be associated with fault slip in order to accommodate asperities present on the plane. This will again be accommodated by the surrounding rock mass inducing stress changes and it will modify the hydraulic aperture of the plane which will affect the pressure distribution in the fault plane. Some of the fluid pressure may also leak into the rock matrix implying a poroelastic response of the rock including both deformation and stress changes. However, in our simulation with 3DEC, we neglect flow and pressure changes within the rock blocks.

It is obvious from the conceptual model described above that fluid injection along fault planes initiates a series of interdependent hydromechanical processes (referred as hydromechanical coupling). These

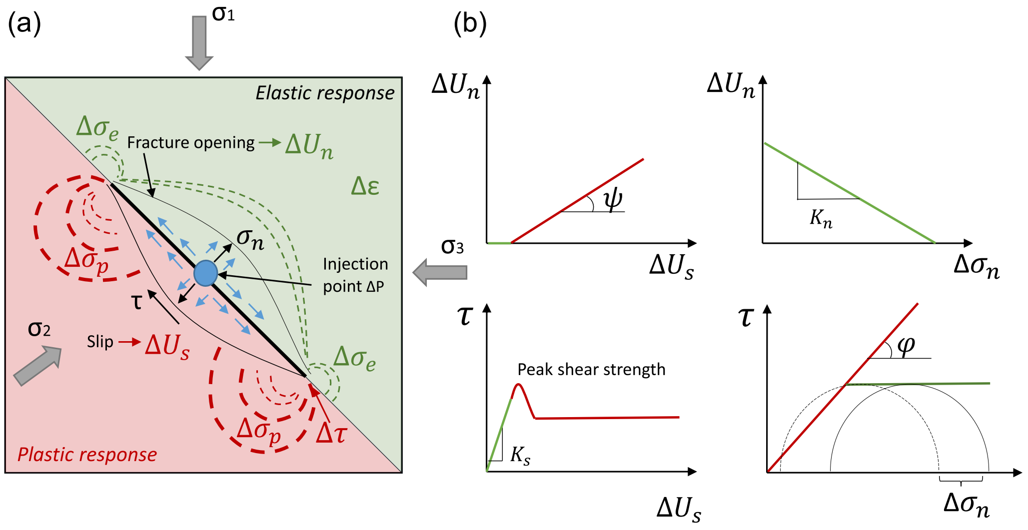

Fig. 3. (a) Stress redistributions around a fracture during elastic and plastic responses (modified from Pollard and Segall, 1987). (b) Main stress-displacement relations, containing fault response to injection, where τ- shear stress, σ- normal stress, ΔU_s- shear displacement, ΔU_n – normal displacement, φ – friction angle, ψ – dilation angle, Δε – rock deformation.

processes that are schematically represented in Fig. 3 will locally affect the stress state and the fracture shape, and thus may change the direction of the local shear traction causing variations of the slip vector orientation. Since stress inversion techniques consist of interpreting this slip vector direction for constraining the in-situ stress state, it is legitimate to ask ourselves about the impact of these processes on in-situ stress estimation from the interpretation of fluid injection data.

3. Methodology

3.1. Background and assumptions of numerical approach

We use the distinct element code 3DEC (Cundall, 1988; Hart et al., 1988) to simulate the fracture as a discontinuity separating two compartments represented as two blocks that are free to move, rotate and separate relative to one another. Here we work with fully coupled hydromechanical simulations, that means that solid deformations influence the fluid pressures and the fluid pressure affect the mechanical stresses and strains. Thus, most of the processes described in our conceptual model above are included in our simulations. The mechanical model in 3DEC is assumed to be quasi-static, meaning that the inertial forces are neglected and the model stays at a state of force equilibrium, or a state of steady flow of material if the model fails.

We assume that the rock blocks are linearly elastic, homogeneous and isotropic. Since we only consider short duration injections into a medium with a strong permeability contrast between the high permeable fracture and the low permeable surrounding rock mass, we consider zero porosity rock blocks such that no fluid diffuses and no poroelastic effects take place in the rock blocks.

Contacts exist between the two deformable blocks at each node of the fracture. The behavior of the fracture is represented by an area contact *Coulomb slip* model (Itasca Consulting Group, 2007). The code uses an explicit algorithm so that information propagates through the model dynamically (time-domain dynamic algorithm). At each time step, the laws of motion and constitutive equations are jointly applied to calculate normal and shear forces at each contact, which then are used in the calculation of the block motion. In the elastic range, the fracture behavior is governed by the fracture normal and shear stiffnesses (units are Pa.m-1), K_n and K_s as described by Eqs. (5) and (6):

$$\Delta F_n = -K_n \Delta U_n A_c \tag{5}$$

$$\Delta F_s = -K_s \Delta U_s A_c \tag{6}$$

where A_c is the contact area, ΔU_n and ΔU_s are the normal and shear displacements increments, ΔF_n and ΔF_s are the normal and shear force increments.

Slip occurs when the force conditions on the plane reach the Mohr-Coulomb criterion:

$$F_{s\ max} = cA_c + F_n \tan \varphi \tag{7}$$

where c and φ are the fracture cohesion and friction angle, respectively. Fracture asperities overriding is captured through a dilation model that is activated when the joint is at slip. The normal displacement ΔU_n leads to a dilation of

$$\Delta U_n(dil) = \Delta U_s \tan \psi \tag{8}$$

where ψ is the dilation angle.

In the model, fluid flow is simulated within the fracture, and not in the surrounding porous medium. The fracture is represented by parallel walls with an equivalent hydraulic aperture u_h. Fluid flowrate per unit width of the idealized fracture follows the cubic law (Witherspoon et al., 1980).

$$q = -\frac{u_h^3 \rho g}{12\mu} \nabla_h = -k_H \nabla_h \tag{9}$$

where k_H is the hydraulic conductivity of the fracture (m/s); ∇_h is the gradient in hydraulic head, ρ is the fluid density (kg/m^3), g is the acceleration due to gravity (m/s^2) and μ is the fluid viscosity (Pa. s).

Coupling Eqs. (8) and (9) implies that in the elastic range, the hydraulic conductivity varies as a function of the effective stress as (Detournay, 1980):

$$k_H = \frac{\rho g}{12\mu}(u_{h0} + \Delta U_n)^3 = \frac{\rho g}{12\mu}\left(u_{h0} + \frac{\Delta F_n}{A_c K_n}\right)^3 = \frac{\rho g}{12\mu}\left(u_{h0} + \frac{\Delta \sigma'_n}{K_n}\right)^3 \tag{10}$$

where u_{h0} is the fracture aperture at zero normal stress and $\Delta\sigma_n{}'$ is the increment in the Terzaghi effective normal stress which is written in simplified form as (Walsh, 1981):

$$\Delta\sigma'_n = \Delta\sigma_n - \alpha \Delta P_p \tag{11}$$

where ΔP_p is the increment in the pore pressure and the effective stress coefficient $\alpha \sim 1$.

In the plastic range, the cubic law is adapted with the hydraulic conductivity of the fracture varying (1) as a function of the effective stress ('elastic' equivalent hydraulic aperture u_{he}) and (2) as a function of dilation induced by fracture slip ('slip' equivalent hydraulic aperture u_{hs}), as

$$k_H = \frac{\rho g}{12\mu}(u_{he} + u_{hs})^3 = \left(u_{h0} + \frac{\Delta \sigma'_n}{K_n} + u_{hs}\right)^3 \tag{12}$$

u_{hs} is simply taken to be equal to the dilation induced at fracture slip $\Delta U_n(dil)$.

3.2. Parameters of the numerical model

The model geometry and conditions are inspired from the conditions at the Mont Terri experiment site. The geometry of the 3DEC model is shown in Fig. 4a. The model's outer boundaries form a cube with edges 20 m long. The model is split into two blocks by a planar joint oriented 140°/60°. There are active and inactive areas of the joint in the model. Active joint area simulates the fracture behavior and is referred as fracture. The radius of the fracture is 5 m. Inactive joint area represents the intact rock and isolates the active fracture area from the model boundaries. Inactive joint areas are prevented from slipping by setting the cohesion and friction values at a high level and elastic parameters are chosen to be compatible with rock mass deformation.

The model is discretized into deformable tetrahedral zones (in total 186,703 zones). The size of the tetrahedral zones in the central part of the block containing the fracture are twice as small as in the region farther from the fracture (0.4 and 0.8 m, respectively). The joint is surrounded by a continuous elastic material.

Equivalent stress and pressure initial and boundary conditions are applied to all model nodes and external model faces, respectively. Principal stress magnitudes were chosen from the Mont Terri estimated in-situ stress state respectively of Martin and Lanyon (2003): $\sigma_{xx} = 3.0$ MPa, $\sigma_{yy} = 5.0$ MPa, $\sigma_{zz} = 6.0$ MPa, and in-situ pore pressure: $pp = 0.5$ MPa. The stresses are aligned with the orientation of the model coordinate axes.

The material properties of the reference model are listed in Table 1. We use two reference models with high and low fracture stiffness values. The high stiffness model contains normal and shear fracture stiffnesses of 500 and 250 GPa/m, when the low stiffness model – 20 and 2 GPa/m, respectively.

Cycles of fluid pressure are applied to a specific flow-knot, located in the middle of the fracture to simulate the injection. Although a fluid pressure of 1.8 MPa would be enough to induce slip on the fracture for the present stress state and plane orientation, we used the initial pressure of 2.0 MPa to increase the velocity of the fluid penetration and facilitate the visualization of the slip results. The following pressure steps were applied with an increment of 0.5 MPa. In total, we applied 6 injection steps. There is no gravity in the model, therefore the pressure

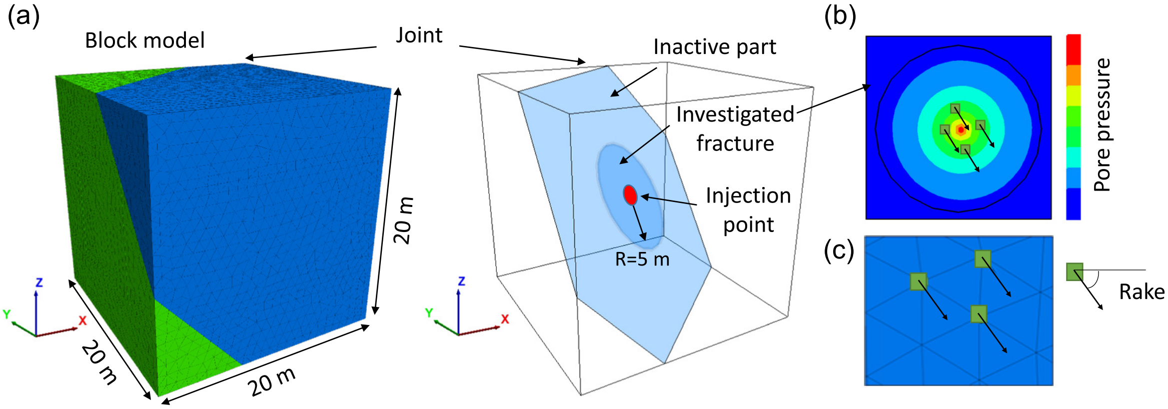

Fig. 4. (a) Three-dimensional model with planar joint, (b) pore pressure distribution and deformation is modeled and tracked for further analyses, (c) sub-contacts (section of the joint) in conditions exceeding the failure conditions (slip) are tracked. The slip direction of the sub-contacts is recorded and its rake direction is computed.

is diffusing radially away from the injection point (Fig. 4b). Initially the fracture is deforming elastically and controlled by the shear and normal stiffness. Eventually, sub-contacts within the joint reach slip conditions (failure). The orientation of the slip vectors of each slipping sub-contact is computed at each time step (Fig. 4c). Time duration of a pressure step is fixed long enough to reach a homogeneous pressure inside the activated fracture patch where all the sub-contacts reach slip conditions.

3.3. Eshelby analytical solution

Because of the fluid pressure gradient imposed by the radial fluid diffusion, we assume that the fracture normal deformation will implicitly lead to an oblate spheroid fracture shape. To estimate the stress perturbation around the spheroidal fracture filled with water we used the analytical solution proposed by Eshelby (1957) for ellipsoidal inclusions. Eshelby's solution is formulated for an infinite, isotropic and linear elastic matrix with an embedded ellipsoidal inhomogeneity referred as the inclusion (Eshelby, 1957, 1961, 1959). The analytical solution provides us with the stresses and strain around an ellipsoidal inclusion. The analytical solution does not capture: (i) transient stress changes associated with fracture tip propagation, (ii) heterogeneous stress distribution inside the inclusion due to the fluid injection. However, it is possible to estimate the direction of the traction force close to the interface between the inclusion and the matrix, which is considered bonded. Here we follow the analytical method proposed by Healy (2009) for a spheroidal inhomogeneity, where the semi axes are $a_1 = a_2 \neq a_3$.

Eshelby derived that the elastic stress inside the inclusion is homogeneous, meaning that it does not depend on the position inside the inclusion. The elastic field inside the inclusion is calculated using the fourth-rank Eshelby tensor that depends on the ellipsoid dimensions and the Poisson's ratio of the matrix (Eshelby, 1957; Mura, 1987) The strain (ε) and stress (σ) are given as following:

$$\varepsilon = \varepsilon^{\mathbf{0}} + \mathbf{S}\colon \varepsilon^{**} \tag{13}$$

$$\sigma = \sigma^{\mathbf{0}} + \mathbf{C}^{\mathbf{0}}\,[\mathbf{S} - \mathrm{I}]\colon \varepsilon^{**} \tag{14}$$

where $\varepsilon^{\mathbf{0}}$ and $\sigma^{\mathbf{0}}$ are the remote homogeneous strain and stresses, respectively, **S** is the Eshelby tensor and I – the identity matrix. The remote strain is related to the remote stress as given by Hooke's Law. The eigen strain ε^{**} is the strain that the inclusion would experience if all the matrix constraints are removed (Mura, 1987). The eigen strain is given by:

$$\varepsilon^{**} = (\mathbf{S} + \mathbf{A})^{-1}\colon (\mathbf{B}\colon \varepsilon^{\mathbf{t}} - \varepsilon^{\mathbf{0}}) \tag{15}$$

where $\varepsilon^{\mathbf{t}}$ is the prescribed eigenvalues, $\mathbf{A} = [\mathbf{C}^{1} - \mathbf{C}^{0}]^{-1}\cdot\mathbf{C}^{0}$, $\mathbf{B} = [\mathbf{C}^{1} - \mathbf{C}^{0}]^{-1}\cdot\mathbf{C}^{1}$, where $\mathbf{C}^{0}$ and $\mathbf{C}^{1}$ are the stiffnesses of the inclusion and the matrix, respectively.

The stress and strain outside the inclusion are given by (Ju and Sun, 2001, 1999)

$$\varepsilon\,(\mathbf{x}) = \varepsilon^{\mathbf{0}} + \mathbf{G}(\mathbf{x})\colon \varepsilon^{**} \tag{16}$$

$$\sigma\,(\mathbf{x}) = \sigma^{\mathbf{0}} + \mathbf{C}^{\mathbf{0}}\cdot\mathbf{G}(\mathbf{x})\colon \varepsilon^{**} \tag{17}$$

where **G(x)** is an another fourth-rank tensor being a function of ellipsoid geometry, Poisson's ratio of the matrix and the coordinate position. To simplify, the Eshelby tensor **S** is the interior-point Eshelby's tensor, and **G(x)** is the exterior-point Eshelby's tensor (see Eshelby, 1957; Healy, 2009; Ju and Sun, 2001, 1999; Meng et al., 2012; Mura, 1987 for details).

Therefore, Eshelby's solution enables fracture to be filled with a material having properties equivalent to water with an elastic modulus of 2.0 GPa, and Poisson's coefficient of 0.49. A spherical oblate ellipsoidal inclusion, representing the fracture opening during the fluid injection, is defined by the ratio of its vertical semi-axis to the horizontal semi-axis. The vertical axis is given by the normal displacement of the fracture, and the horizontal – by its radius.

Table 1
Properties of the numerical model.

Block		Joint	*Active part*	*Inactive part*
Mass density [kg/m^3]	2450	Normal stiffness [GPa/m]	500 (or 20)	500 (or 20)
Bulk modulus [GPa]	5.9	Shear stiffness [GPa/m]	250 (or 2)	250 (or 2)
Shear modulus [GPa]	2.3	Friction angle [°]	22	40
Fluid		Cohesion [MPa]	0	1×10^{24}
Fluid density [kg/m^3]	1000	Aperture, [m]	1×10^{-6}	
Bulk modulus [GPa]	2			
Viscosity [Pa.s]	0.01			

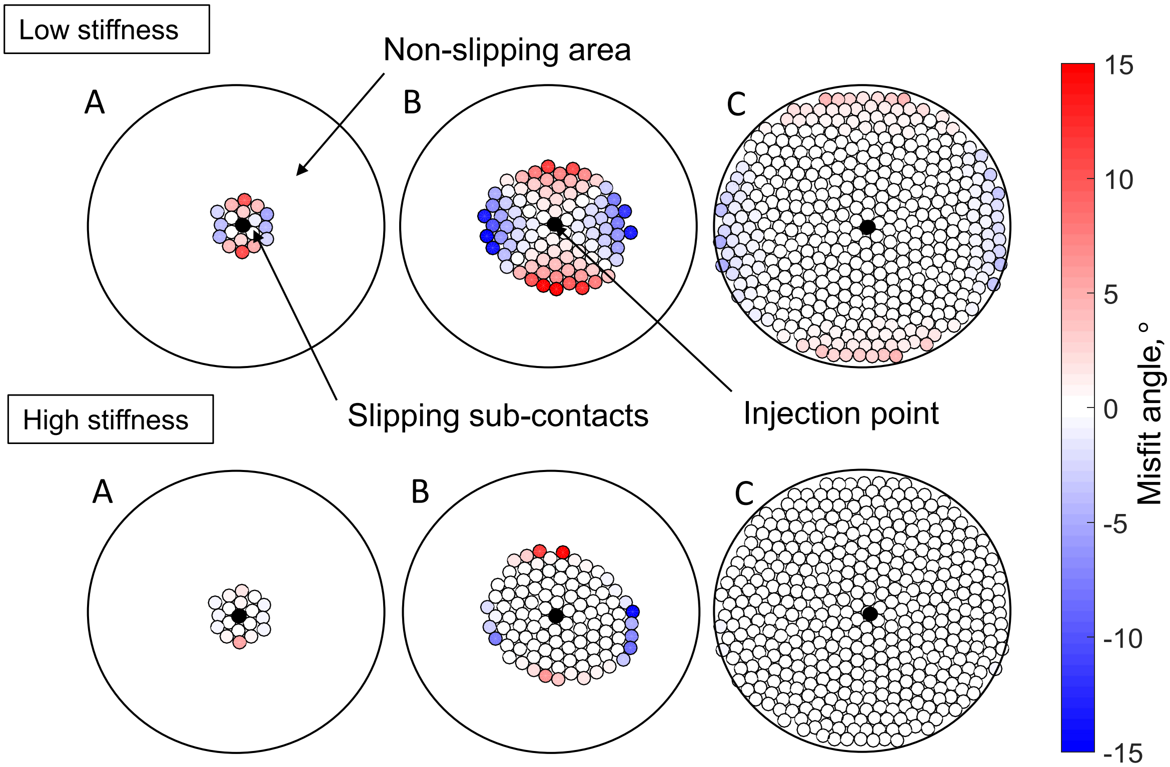

Fig. 5. Misfit angle of the fractures with low and high stiffnesses at different diffusion stages of the activated patch growth: A – In the beginning of the pressurizing, B – in the middle and C – in the end of pressurizing. For the exact time of A, B, C refer to the Fig. 6. Fracture radius – 5 m.

4. Results

4.1. Numerical and analytical misfit angle

For the stress state and geometry of the reference case presented above, the orientation of the resolved shear stress predicted by the Wallace-Bott hypothesis has a rake angle of 43°. The misfit angle of slipping sub-contacts between the predicted WB orientation and the numerical 3DEC orientation for the first pressure step of 2 MPa is shown in Fig. 5. In the beginning of the pressurizing (Fig. 5A), slipping sub-contacts are only observed very close to the injection point. The closer the sub-contact is located to the injection point, the less misfit angle is observed. The sub-contacts of the low stiffness model show the misfit up to 15°, while the misfit angles of the high stiffness model are below 5°. With fluid diffusion into the fracture, the slipping area grows (Fig. 5B). For both models the slip direction deviation from the WB hypothesis is primarily occurring close to the activated fracture patch tip (Fig. 5B), where the strain gradient (or the aperture gradient) is higher and, thus, the stress perturbation is the most severe. However, in comparison to the high stiffness model, the low stiffness model shows the gradual increase of the deviation from the injection point to the fracture tips. This observation occurs due to the higher deformability of the low stiffness fracture that induces larger intact rock deformation. At the end of the pressure step all sub-contacts for both models achieve slipping conditions. A deviation $< 5°$ is still observed on the tips of the low stiffness fracture, while all the slip vectors of the high stiffness fracture are consistent with the predicted value by the Wallace-Bott hypothesis.

To avoid the boundary effects and investigate only the effect of the fluid pressure on the slip deviation, in the following section we analyzed the orientation of the slip vectors for both vectors with a 3 m activated patch radius. The summary of the misfit angles measured away from the fracture boundaries at every time step is shown in Fig. 6. Firstly, it is demonstrated that the first activated sub-contact located at the injection point is consistent with the WB hypothesis for the high stiffness model and deviates for the low stiffness model. In the low stiffness case, as the fluid diffuses into the fracture the misfit angle tends towards zero (i.e., towards the WB predicted vector), while the slip vector of the high stiffness fracture stays consistent with the WB predicted vector. The same tendency is observed later for activated sub-contacts for both models: with time, the deviated vectors become consistent with the WB predicted vectors. For the visualization of the misfit angles we used the range of ± 30°, because the principal misfit angles are in this range. However, we observed an individual sub-contact starting deviation at $-90°$ in the beginning of the pressurizing for the low stiffness fracture, meaning that the deviation is observed at the very beginning of the pressurizing at the location of the injection for the low stiffness fracture. The high stiffness fracture does not show the deviation at the beginning of the pressurizing. At the same time the magnitude of the slipping vectors increases with fluid diffusion. Fig. 6 shows that the vector deviation decreases with the increasing magnitude. Moreover, all vectors consistent with the WB hypothesis have a slip magnitude of > 1 μm. The deviated vectors in the low stiffness model have larger slip magnitudes (typically > 1 μm) than the deviated vectors in the high stiffness model (typically < 0.1 μm).

Secondly, the stiffness difference results in the speed difference of the rupture propagation along the fracture plane: propagation is quicker for the low stiffness model. This is observed because here the 3DEC simulation is pressure controlled, meaning that for the same pressure step, a larger fluid volume is required to maintain the pressure step in the low stiffness model compared to the high stiffness one (This volume depends on the fracture aperture and on the rock mass properties). Consequently, the high stiffness model takes more time to fulfill the fracture.

Thirdly, Fig. 6 shows that once the fracture is filled with the fluid (at the first pressure step of 2 MPa), the slip deviation does not increase for the higher-pressure injections. The slip direction becomes constant and consistent with the WB hypothesis.

The shape of the activated fracture patch of 3 m, which is related to

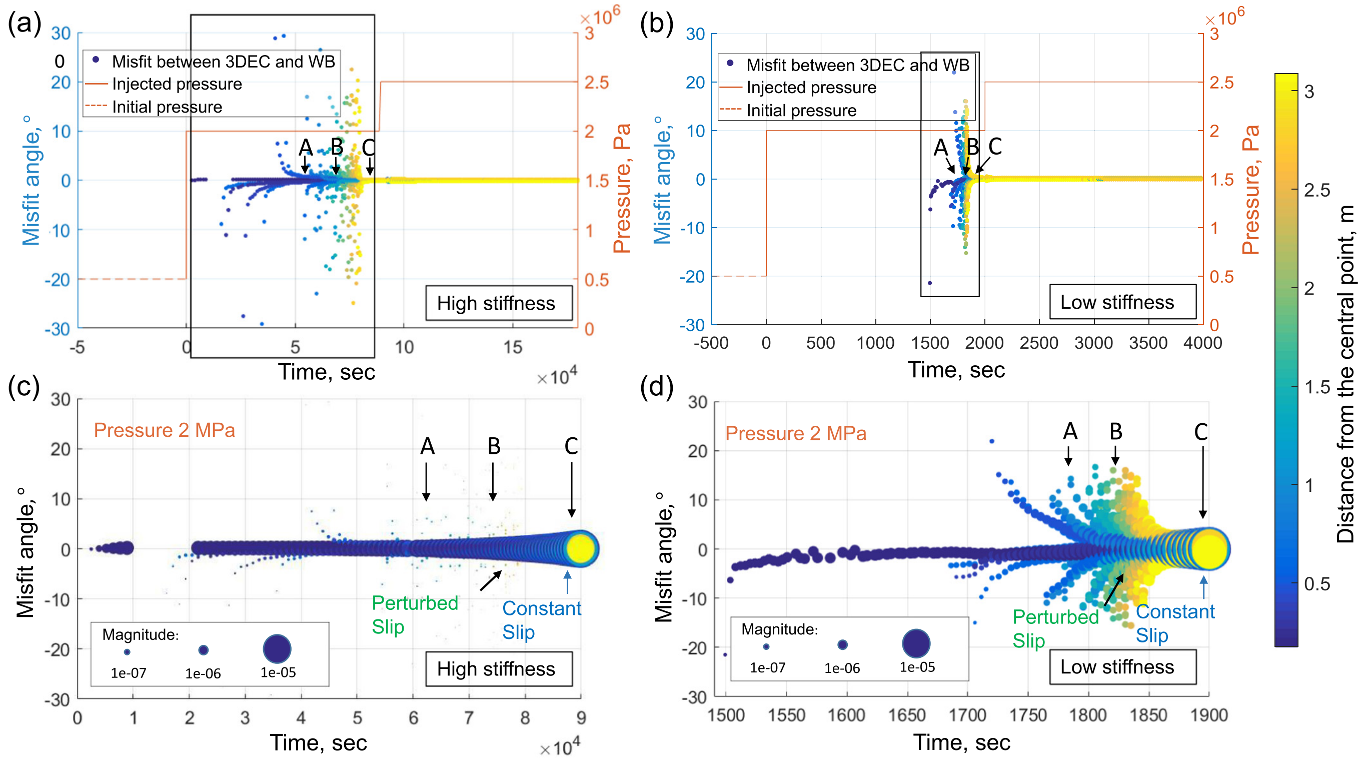

Fig. 6. Misfit angle for the high (a, c) and low (b, d) stiffness model with increasing injection pressure. Figures (c) and (d) is a zoomed-in part with slipping vectors magnitudes corresponding to rectangles in (a) and (b). The number of points corresponds to the amount of the slipping sub-contacts within the fracture, and the color indicates the distance of these sub-contacts from the injection point. A, B, C – different diffusion stages of the investigated activated patch in Fig. 5.

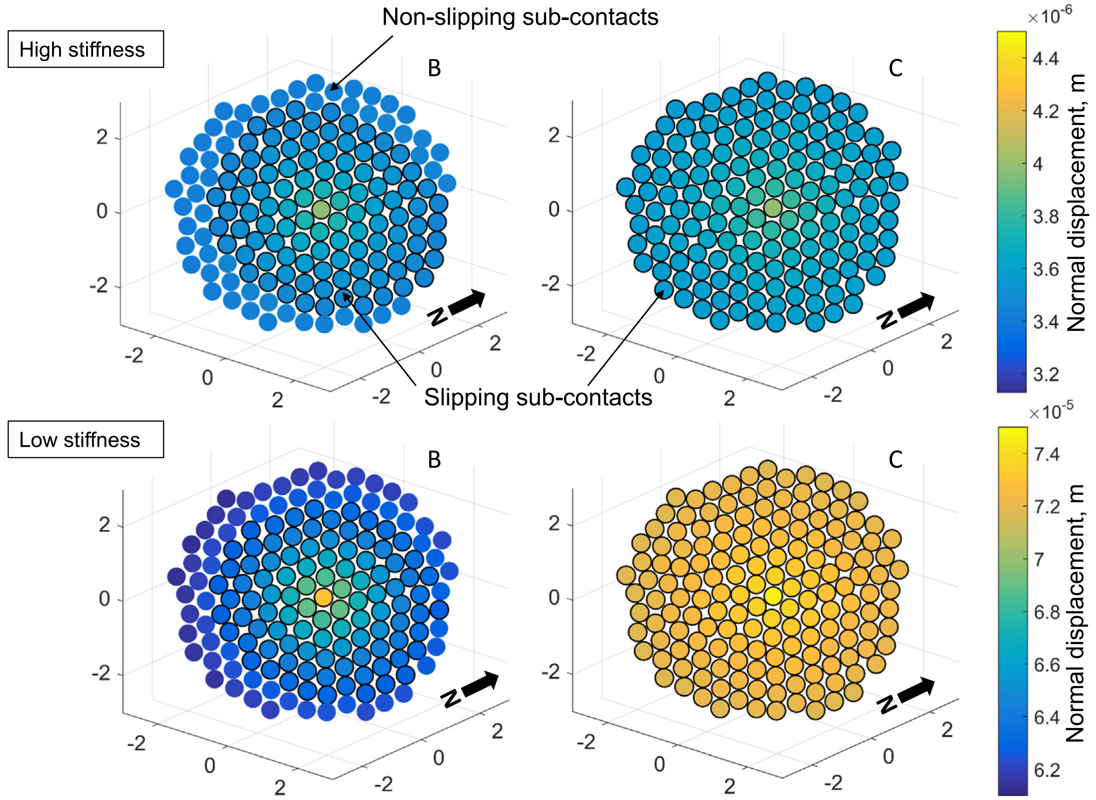

Fig. 7. Fracture normal displacement for the high and low stiffness models computed at the time of B and at the time C. The black circles indicate the slipping sub-contacts. Axis scale is in meters.

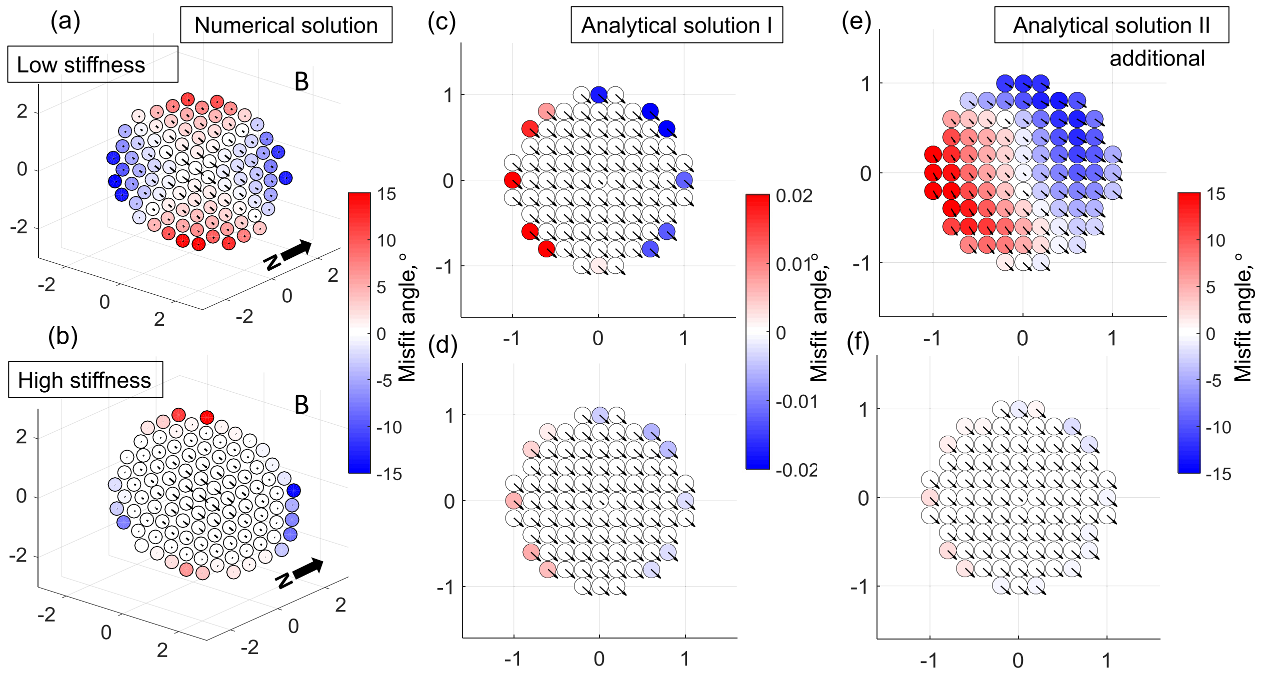

Fig. 8. The directions (black arrows) of the resolved shear on the low (a) and high (b) stiffness numerical and analytical models. On the analytical model I the real apertures of the low (c) and high (d) stiffness fracture are represented, on the analytical model II - the increased apertures of the low (e) and high (f) stiffness fractures for visualization. The sub-contacts on the fractures (a) and (b) correspond to the slipping sub-contacts at the diffusion stage B on the high and low stiffness fractures in Fig. 7. Axis scale is in meters.

the distribution of the fracture aperture under the pressure diffusion of 2 MPa is illustrated in Fig. 7. Normal displacement of both high and low stiffness fractures gradually decreases from the injection point to the tips at the diffusion stage B, and become close to uniform at the diffusion stage C. However, it is important to note that the normal displacement of the low stiffness fracture is about 20 times higher in magnitude than the normal displacement of the high stiffness fracture. The normal stiffness is 25 times higher, but we compare the activated patched in terms of the size of the activated patch, not the time, therefore, the obtained ratio differs from the stiffness ratio. These results clearly indicate that the fracture planes change their shape with time and fluid diffusion. The central patch of the fracture, close to the point source of fluid injection, becomes more planar at the diffusion stage C in comparison to the diffusion stage B for both high and low stiffness models.

The Eshelby (1957) analytical solution demonstrated the effect of these changes in the fracture shape on the slip deviation. Fig. 8 compared the numerical and analytical solution for both models at the time B. Based on results of Fig. 7, we represented the fracture shape as an oblate spheroid with a ratio of its vertical semi-axis to the horizontal semi-axis of $(1.17 \times 10^{-5})/3$ for the low stiffness fracture, $(5.9 \times 10^{-7})/3$ for the high stiffness fracture. The vertical semi-axis of the oblate spheroids correspond to the absolute value of the normal displacements at the diffusion stage B (Fig. 7). The analytical solution for such a "penny-shaped" fracture gives the misfit angle $\ll 1^{\circ}$ and the distribution of the misfit angles looks different to the numerical solution. However, if we compare the analytical solution for the low and high stiffness models, it is clearly observed that the curved fracture surfaces corresponding to the low stiffness fracture show higher misfit than the planar surfaces corresponding to the high stiffness fracture. In addition we adapted the shape of the analytical fracture in order to have the maximum misfit angle of $\pm 15^{\circ}$ for the high stiffness model. To do so, we increased the ratio values in both models by 10^5, so that the ratio is 0.39 for the low stiffness model and 0.02 for the high stiffness model. When the fracture becomes more ellipsoidal in comparison to the previous "penny-shaped", again it can be seen that the more oblate fracture shape causes high slip deviation. This is the important result given by the Eshelby solution, that the shape of the pressure-activated patch can significantly impact the orientation of the slip vector.

4.2. *Sensitivity analysis*

Since the deviation is observed only at the initial pressure step of 2.0 MPa, the sensitivity study for both high and low stiffness models covering (i) dilation, (ii) friction angle and (iii) aperture was performed at this pressure step. The fracture properties used in the sensitivity study are given in Table 2.

The results of the study are shown in Fig. 9. For the friction angle and fracture aperture the investigation was made until all the sub-contacts will only grow in magnitude. As has been shown above, after the fracture is filled with water the slip orientation becomes closer to the theoretical value.

4.2.1. *Dilation angle*

The effect of joint dilation is illustrated in Fig. 9(a, b). For the low stiffness model, high dilation increases deviation by approximately 1° in the beginning of the pressurization and accelerates the time for the severe deviation. The same effect of acceleration is observed for the high stiffness model: the orientation of the slipping vectors of the high stiffness model with $\psi = 30$ become closer to the WB predicted value much earlier than for $\psi = 0$. The same slip magnitude is achieved much earlier for fractures with a lower dilation angle. The range of the misfit angle and the slip magnitude of the deviated vectors for both models

Table 2
Fracture properties used in the sensitivity study.

Fracture properties	Test values		
Stiffness, [GPa/m]	K_n = 500, K_s = 250	K_n = 20, K_s = 2	
Friction angle, [°]	22	19	16
Dilation angle, [°]	0	15	30
Aperture, [m]	1×10^{-6}	1×10^{-5}	1×10^{-7}

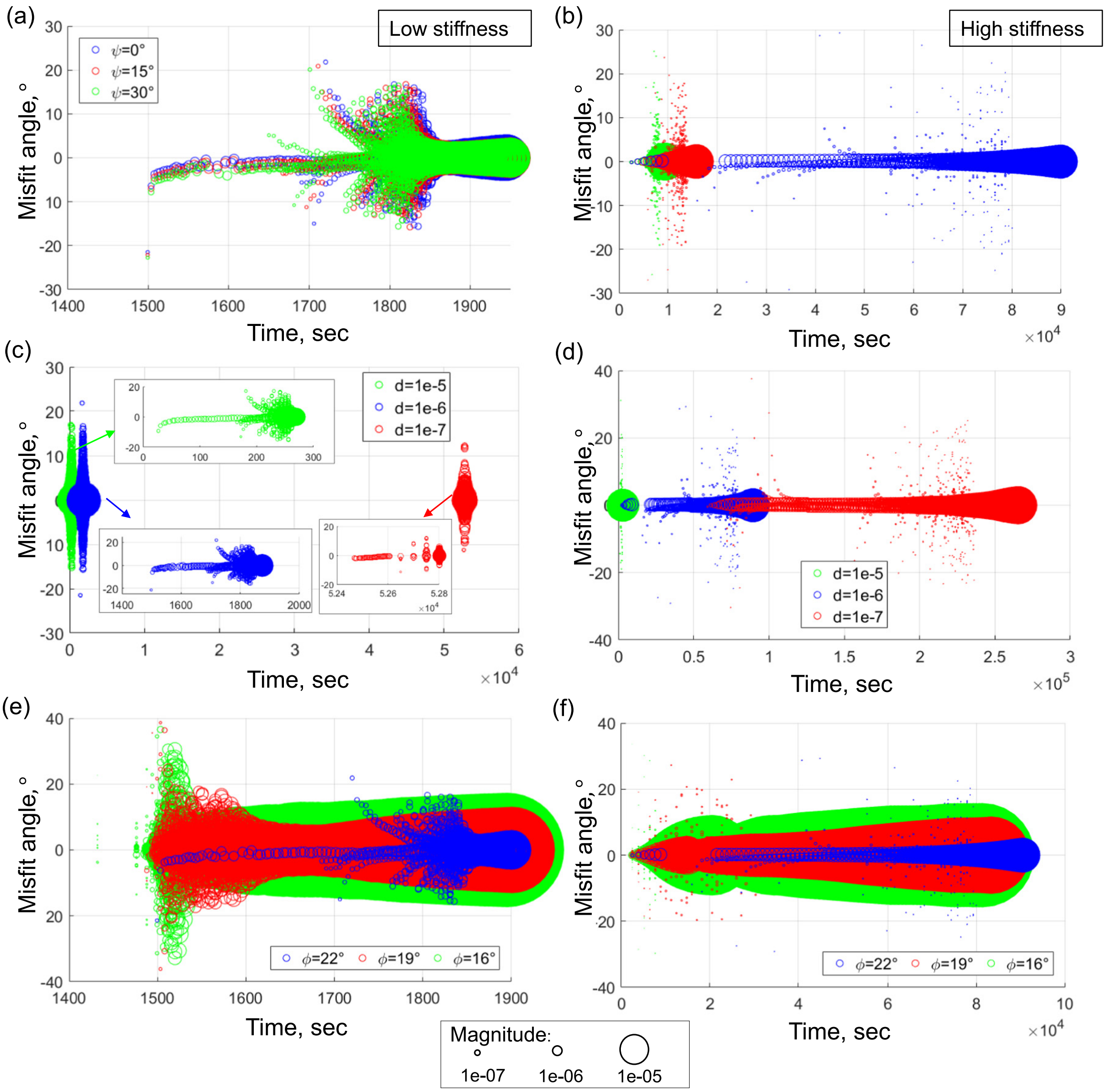

Fig. 9. Sensitivity study. Similarly to Fig. 6, we show here the misfit angle between the modeled slip and the expected slip according to the WB hypothesis (Misfit angle). a), b) - effect of dilation angle, c), d) - effect of initial aperture, and e), f) - effect of friction angle.

does not significantly vary between models with different dilation values. Therefore, for the tested conditions it can be said that dilation does not affect significantly the misfit angle between the slip directions and the WB theoretical angle for both models.

4.2.2. Fracture hydraulic aperture

The size of the fracture aperture affects its permeability and consequently the time of fluid diffusion into the fracture. It is clearly observed in Fig. 9(c, d) that for the smaller aperture of 10 μm for both high and low stiffness models it takes more time to fill a fracture with a fluid and achieve non-deviated vectors on the whole fracture. The range of the misfit angles for the low stiffness model is smaller and the time during which slip activation is longer for the lowest aperture case (0.1 μm). The discontinuities in the lowest aperture case arise due to the increased time step applied by the 3DEC to capture the slip orientation. However, the tendency of deviation is preserved – the deviated vectors tend to achieve the constant value consistent with the predicted WB orientation. After a certain amount of time (depending on the aperture size) the slip becomes consistent with the theoretical value. However, the longer it takes for fluid injection to propagate inside the fracture, the longer we observe the misfit.

4.2.3. Frictional angle

Friction angles of 16° and 19° were tested and compared to the base case of 22°. Friction angle has the strongest effect on the misfit angle of all the tested parameters in the sensitivity analysis (Fig. 9e, f). For the low stiffness model the friction angle of 16° causes the slip deviation up to ± 40°, the friction angle of 19° - the slip deviation of ± 25°, for the friction angle of 22° - deviation of 20°. For the high stiffness model the misfit range does not change significantly for the tested values of the friction angle.

A lower friction angle also accelerates the severe deviation of slip and increases the slip magnitude of the deviated vectors. Generally, the change in friction angle induces a significant change in the slip directions. For the low stiffness model it increases the misfit angle and the magnitude of the deviated vectors. For the high stiffness model it does not significantly increase the misfit or the magnitude of the deviated vectors. These results demonstrate that the friction angle plays a significant role in slip deviation for the present conditions.

The sensitivity study demonstrates that (i) for all of the tested cases the slip reaches a constant direction that is consistent with the WB hypothesis when the activated patch gets larger and is filled with water, (ii) the longer it takes for fluid injection to propagate inside the fracture, the longer we observe the misfit, (iii) dilation and aperture do not significantly affect the slip orientation, while the friction angle and the stiffness are key parameters influencing the misfit angle.

5. Discussion

The WB hypothesis is generally used to estimate stress state using stress inversion methods. However, it is known that many of the assumptions of the hypothesis are not respected in field cases. In this study we show, that a non-uniform pressure field induced by a local fluid injection in a planar fault can significantly deviate the slip vector orientation from the WB prediction, which is consistent with previous studies (Martínez-Garzón et al., 2016; Terakawa et al., 2012). The injection of fluid pressure affects the three-dimensional fracture shape causing a complex stress perturbation at the tip between the activated fracture patch and the remaining inactive zone of the fracture.

Generally, when fluid diffuses into the fracture and triggers the slip on sub-contacts, their primary orientation deviates from the WB predicted direction. With continued fluid propagation their orientation rotates towards the WB predicted value. After a given injection time the slip becomes constant on all the fracture sub-contacts and consistent with the WB hypotheses.

The primary deviation and then agreement of the slipping vectors with the WB predicted value is connected with the fracture shape during the pressurizing. The highest deviation is related to the sharp aperture gradient that dynamically propagates at the tip of the activated patch. After this patch was activated the fluid then filled the fracture, reducing the aperture gradient and uniformly aligning the slip orientation.

The fracture shape and propagation depend on the fracture stiffness. A high stiffness fracture tends to minimize deformation normal to the fracture. Therefore, the fracture opening is small, it does not deform the surrounded rock mass, and the deviation is only observed at the tip of the activated patch because of the inherent aperture difference and stress perturbation on the fracture tips. The slip vectors on the major part of the activated patch are mostly consistent with the WB predicted orientations. These results confirm the observations obtained by Dupin et al. (1993), who used the high fracture stiffness to validate the Wallace-Bott hypothesis using 3DEC. A low stiffness fracture deforms progressively towards the tips. As a result, gradual slip deviation towards the fracture tips is observed due to the higher distortion induced on the medium close to the fracture tip. Hence, more sub-contacts deviate during the fluid injection on the low stiffness fracture. However, for both stiffness models the direction of the slipping vector close to the injection point located in the central part of the activated fracture patch is consistent with the WB prediction.

The numerical 3DEC and the analytical WB models gave very different results in terms of the misfit angle value and its distribution on the fracture plane. The fully coupled 3DEC numerical solution estimates the stress perturbation considering the pressure gradient inside the fracture, the fracture deformation and transient stress changes associated with fracture tip propagation. The analytical solution estimates the stress perturbation based only on the shape of the inclusion. The Eshelby analytical solution does not consider internal stress perturbations, the interface between the inclusion and the matrix is considered bonded and friction properties of the fracture. The analytical solution is made for a perfect ellipsoid, whereas an activated patch in 3DEC has a shape more like a “bell”. The numerical solution is calculated on the tetrahedral mesh, while the analytical was applied on a simple square grid. It can be concluded that the numerical model takes more aspects into account and its results are more reliable. However, the Eshelby solution helped in understanding the effect of the shape of the activated patch on the slip deviation and these results are very important. The comparison of the numerical and analytical solutions for the low and high stiffness model indicates that the more the fracture is deformed the more it causes the deviation.

The sensitivity analyses demonstrate that the friction angle has a strong influence on slip deviation in the low stiffness model, which is consistent with the results obtained by Pascal (2002). The misfit of the high stiffness model does not change systematically with friction angle, which could be due to the high rigidity of non-deformable fracture planes. Lejri et al. (2015) also concluded that increasing friction will decrease the slip magnitude as well as the misfit angle until the slip vectors become consistent with the WB hypothesis. In this study, the slip magnitude indeed decreases with increasing friction, which is consistent with Lejri et al. (2015).

All our observations indicate that the observed slip deviation is probably generated by the stress perturbations associated with the non-uniform deformation induced by the non-uniform pressure distribution. The comparison between the analytical and numerical solutions suggests that the shape of the fracture cannot explain fully the value of the misfit angle. The numerical solution, which considers both shape and pressure changes in the fracture, demonstrated that the non-uniform fluid pressure contributes to the misfit angle. It is probable that the misfit angle depends on additional parameters that are not considered in this study. The FS data shows that the orientation of the slip vectors rotates. These field observations are consistent with our numerical observations from the low stiffness model, (the Opalinus clay in Mont Terri shale rocks has relatively low stiffness). The sub-contacts deviate from the WB assumptions as soon as they are activated and then constantly rotate their direction parallel to the WB predicted value. The interruptions in the constant trajectory of slip rotations and, in general its deviation may be explained by the fact that the deviation occurs with injection time, and sharp changes in the fault opening with time could be potentially related to friction or stiffness variations, which are found to be the main parameters affecting the slip deviation in the present study. Fracture deformation might allow for a fracture initially unfavorably oriented towards stress to slip locally. This can propagate a weakening patch in the fracture and finally lead to larger slip, which is not yet predictable by the WB hypothesis. In addition, the slip directions varying with time may also have other explanations such as different asperities on the fracture, fracture curvature, activation of several fractures at the same time and other reasons that have not been studied in this paper.

The constant slip on all the fracture sub-contacts of the numerical model and its consistence with the WB hypothesis may be related to the numerical model boundary conditions and geometry. A larger model incorporating more realistic fractures or faults might produce larger deviation from the WB prediction compared to our study. In addition, the accuracy of the 3DEC model can also be improved by testing different meshing size and fracture scale, but this would require significantly more computational power.

6. Conclusion

The data obtained from the FS experiment in Mont Terri showed the rotation of the slip vectors during the fluid injection. To understand the origin of this rotation and possibility of using these vectors in the stress inversion methods we checked the fundamental assumption that slip is parallel to the resolved shear stress in the presence of a local fluid source such as a borehole injection across a fracture. In this study we thus focused on the validation of the WB hypothesis in the presence of a fluid point source that may induce slip reorientations using analytical and numerical methods.

We built two numerical models consisting of a homogeneous, isotropic, elastic and deformable block with an embedded low stiffness/high stiffness fracture using the 3DEC numerical method. We inject a fluid pressure step-by-step to trigger the slip along the fracture. The main result of this analysis is that for a given homogeneous far-field stress in all tested cases, we calculate that a non-uniform pressure field induced by fluid injection does affect the slip direction. The effect is different for a low stiffness/high stiffness fracture and based on the fracture deformation and propagation during the fluid diffusion. The high stiffness fractures are more consistent with the Wallace-Bott theoretical solution, while the low stiffness fractures demonstrate the significant deviation. The sensitivity analysis show that among all the tested parameters, the stiffness and friction angle are the key factors influencing the misfit angle between the numeral observations and the theoretical WB values.

Therefore, the estimation of stresses based on the slip directions of activated fractures during borehole injection is not explicit. The fracture stiffness should be always considered and the slip direction calculated for a longer pressure injection. Based on the results obtained from the investigated numerical model, for the Mont Terri experimental site we propose to make a stress inversion only when the slip has a constant orientation during a significant time of pressurization.

Acknowledgements

The authors would like to thank the Itasca Consulting Group for providing with the software licensing in the frame of the Itasca Education Partnership (IEP) Program. Many thanks to the mentor of the program – Dr. Damjanac for his assistance and cooperation. We are grateful for the constructive comments of Richard Lisle and Frantz Maerten, who helped us to substantially improve our manuscript. This work is funded by the University of Neuchatel and by Swisstopo via the Mont Terri Consortium.

References

Allmendinger, R.W., Cardozo, N., Fisher, D.M., 2011. Structural Geology Algorithms: Vectors and Tensors. Cambridge University Press.

Anderson, E.M., 1951. The Dynamics of Faulting and Dyke Formation With Applications to Britain, 2nd ed. Oliver and Boyd, Edinburgh.

Angelier, J., 1975. Sur l'analyse de mesures recueillies dans des sites faillés: l'utilité d'une confrontation entre les méthodes dynamiques et cinématiques. CR Acad. Sci 281, 1805–1808.

Angelier, J., 1979. Determination of the mean principal directions of stresses for a given fault population. Tectonophysics 56, T17–T26. https://doi.org/10.1016/0040-1951(79)90081-7.

Angelier, J., 1990. Inversion of field data in fault tectonics to obtain the regional stress—III. A new rapid direct inversion method by analytical means. Geophys. J. Int. 103, 363–376.

Angelier, J., Colletta, B., Anderson, R.E., 1985. Neogene paleostress changes in the Basin and Range: a case study at Hoover Dam, Nevada-Arizona. Geol. Soc. Am. Bull. 96, 347–361.

Arthaud, F., 1969. Méthode de détermination graphique des directions de raccourcissement, d'allongement et intermédiaire d'une population de failles. Bull. la Société géologique Fr. 7, 729–737.

Barrier, E., Angelier, J., 1986. Active collision in eastern Taiwan: the Coastal Range. Tectonophysics 125, 39–72. https://doi.org/10.1016/0040-1951(86)90006-5.

Bergerat, F., 1987. Stress fields in the European platform at the time of Africa-Eurasia collision. Tectonics 6, 99–132. https://doi.org/10.1029/TC006i002p00099.

Blenkinsop, T., Lisle, R., Ferrill, D., 2006. Introduction to the special issue on new dynamics in palaeostress analysis. J. Struct. Geol. 28 (6), 941–942.

Bott, M.H.P., 1959. The mechanics of oblique slip faulting. Geol. Mag. 96, 109–117.

Carey, E., 1976. Analyse numérique d'un modèle mécanique élémentaire appliqué à l'étude d'une population de failles: calcul d'un tenseur moyen des contraintes à partir des stries de glissement. Thèse de troisième cycle. Univ. Paris-Sud, Orsay.

Carey, E., Brunier, B., 1974. Analyse théorique et numérique d'un modèle mécanique elementare appliqué à l'étude d'une population des failles. C. r. Acad. Sci. Paris, sér. D 279, 397–400.

Cérérier, B., Etchecopar, A., Bergerat, F., Vergely, P., Arthaud, F., Laurent, P., 2012. Inferring stress from faulting: from early concepts to inverse methods. Tectonophysics 581, 206–219. https://doi.org/10.1016/J.TECTO.2012.02.009.

Cornet, F.H., Julien, P., 1989. Stress determination from hydraulic test data and focal mechanisms of induced seismicity. Int. J. Rock Mech. Min. Sci. Geomech. Abstr. 26, 235–248. https://doi.org/10.1016/0148-9062(89)91973-6.

Cundall, P.A., 1988. Formulation of a three-dimensional distinct element model—part I. A scheme to detect and represent contacts in a system composed of many polyhedral blocks. Int. J. Rock Mech. Min. Sci. Geomech. Abstr. 25, 107–116. https://doi.org/10.1016/0148-9062(88)92293-0.

Delvaux, D., Sperner, B., 2003. New aspects of tectonic stress inversion with reference to the TENSOR program. Geol. Soc. London, Spec. Publ. 212, 75–100. https://doi.org/10.1144/GSL.SP.2003.212.01.06.

Detournay, E., 1980. Hydraulic conductivity of closed rock fracture: an experimental and analytical study., in: Can Rock Mech Symp Proc 13th, Underground Rock Eng, The HR Rice Mem Symp. CIM.

Dupin, J.M., Sassi, W., Angelier, J., 1993. Homogeneous stress hypothesis and actual fault slip: a distinct element analysis. J. Struct. Geol. 15, 1033–1043. https://doi.org/10.1016/0191-8141(93)90175-A.

Ellsworth, W.L., 2013. Injection-induced earthquakes. Science. 341 (6142), 1225942.

Eshelby, J.d., 1957. The determination of the elastic field of an ellipsoidal inclution and related problems. Proc. Phys. Soc. London, Ser. A 241, 376–396. https://doi.org/10.1098/rspa.1983.0054.

Eshelby, J.D., 1959. The elastic field outside an ellipsoidal inclusion. Proc. R. Soc. Lond. A 252, 561–569.

Eshelby, J.D., 1961. Elastic inclusions and inhomogeneities. Prog. solid Mech. 2, 89–140.

Etchecopar, A., Vasseur, G., Daignieres, M., 1981. An inverse problem in microtectonics for the determination of stress tensors from fault striation analysis. J. Struct. Geol. 3, 51–65.

Evans, K.F., Zappone, A., Kraft, T., Deichmann, N., Moia, F., 2012. A survey of the induced seismic responses to fluid injection in geothermal and CO2reservoirs in Europe. Geothermics 41, 30–54. https://doi.org/10.1016/j.geothermics.2011.08.002.

Gephart, J.W., Forsyth, D.W., 1984. An improved method for determining the regional stress tensor using earthquake focal mechanism data: application to the San Fernando earthquake sequence. J. Geophys. Res. Solid Earth 89, 9305–9320.

Guglielmi, Y., 2016. Mont Terri Project. Technical note 2015-60. Phase 21. In-situ clay faults slip hydro-mechanical characterizatiom (FS experiment), Mont Terri underground rock laboratory.

Guglielmi, Y., Cappa, F., Hervé, @bullet, @bullet, L., Janowczyk, J.B., Rutqvist, J., Tsang, @bullet C F, Wang, @bullet J S Y, 2013. ISRM Suggested Method for Step-Rate Injection Method for Fracture In-Situ Properties (SIMFIP): Using a 3-Components Borehole Deformation Sensor. doi:https://doi.org/10.1007/s00603-013-0517-1

Guglielmi, Y., Cappa, F., Amitrano, D., 2008. High-definition analysis of fluid-induced seismicity related to the mesoscale hydromechanical properties of a fault zone. Geophys. Res. Lett. 35, 1–6. https://doi.org/10.1029/2007GL033087.

Guglielmi, Y., Birkholzer, J., Rutqvist, J., Jeanne, P., Nussbaum, C., 2017. Can fault leakage occur before or without reactivation? Results from an in situ fault reactivation experiment at Mont Terri. Energy Procedia 114, 3167–3174. https://doi.org/10.1016/j.egypro.2017.03.1445.

Hancock, P.L., 1985. Brittle microtectonics: principles and practice. J. Struct. Geol. 7, 437–457.

Hansen, J.A., 2013. Direct inversion of stress, strain or strain rate including vorticity: a linear method of homogenous fault-slip data inversion independent of adopted hypothesis. J. Struct. Geol. 51, 3–13. https://doi.org/10.1016/j.jsg.2013.03.014.

Hart, R., Cundall, P.A., Lemos, J., 1988. Formulation of a three-dimensional distinct element model—part II. Mechanical calculations for motion and interaction of a system composed of many polyhedral blocks, in: International Journal of Rock Mechanics and Mining Sciences & Geomechanics Abstracts. Elsevier, pp. 117–125.

Healy, D., 2009. Elastic field in 3D due to a spheroidal inclusion—MATLAB™ code for Eshelby's solution. Comput. Geosci. 35, 2170–2173.

Itasca Consulting Group, 2007. Inc. 3DEC (Three-Dimensional Distinct Element Code), Version 5. MN, Minneapolis, pp. 0.

Jaeger, J.C., Cook, N.G.W., Zimmerman, R., 2009. Fundamentals of Rock Mechanics. John Wiley & Sons.

Jaeggi, D., Laurich, B., Nussbaum, C., Schuster, K., Connolly, P., 2017. Tectonic structure of the "Main Fault" in the Opalinus Clay, Mont Terri rock laboratory (Switzerland). Swiss J. Geosci. 110, 67–84. https://doi.org/10.1007/s00015-016-0243-2.

Ju, J.W., Sun, L.Z., 1999. A novel formulation for the exterior-point Eshelby's tensor of an ellipsoidal inclusion. J. Appl. Mech. 66, 570–574. https://doi.org/10.1115/1.2791090.

Ju, J.W., Sun, L.Z., 2001. Effective elastoplastic behavior of metal matrix composites containing randomly located aligned spheroidal inhomogeneities. Part I: Micromechanics-based formulation. Int. J. Solids Struct. 38, 183–201. https://doi.org/10.1016/S0020-7683(00)00023-8.

Kaven, J.O., Maerten, F., Pollard, D.D., 2011. Mechanical analysis of fault slip data: Implications for paleostress analysis. J. Struct. Geol. 33, 78–91. https://doi.org/10.1016/J.JSG.2010.12.004.

Lacombe, O., Angelier, J., Laurent, P., Bergerat, F., Tourneret, C., 1990. Joint analyses of calcite twins and fault slips as a key for deciphering polyphase tectonics: Burgundy as a case study. Tectonophysics 182, 279–300. https://doi.org/10.1016/0040-1951(90)90168-8.

Laurich, B., Urai, J.L., Desbois, G., Vollmer, C., Nussbaum, C., 2014. Microstructural evolution of an incipient fault zone in Opalinus Clay: Insights from an optical and electron microscopic study of ion-beam polished samples from the Main Fault in the Mt-Terri Underground Research Laboratory. J. Struct. Geol. 67, 107–128. https://doi.org/10.1016/j.jsg.2014.07.014.

Le Pichon, X., Bergerat, F., Roulet, M.-J., 1988. Plate kinematics and tectonics leading to the Alpine belt formation; a new analysis. Geol. Soc. Am. Spec. Pap. 218, 111–132.

Lejri, M., Maerten, F., Maerten, L., Soliva, R., 2015. Tectonophysics Paleostress inversion: a multi-parametric geomechanical evaluation of the Wallace – Bott assumptions. Tectonophysics 657, 129–143. https://doi.org/10.1016/j.tecto.2015.06.030.

Lejri, M., Maerten, F., Maerten, L., Soliva, R., 2017. Accuracy evaluation of both Wallace-Bott and BEM-based paleostress inversion methods. Tectonophysics 694, 130–145. https://doi.org/10.1016/j.tecto.2016.11.039.

Letouzey, J., 1986. Cenozoic paleo-stress pattern in the Alpine Foreland and structural interpretation in a platform basin. Tectonophysics 132, 215–231. https://doi.org/10.1016/0040-1951(86)90033-8.

Liesa, C.L., Simón, J.L., 2009. Evolution of intraplate stress fields under multiple remote compressions: the case of the Iberian Chain (NE Spain). Tectonophysics 474, 144–159.

Lisle, R.J., 1992. New method of estimating regional stress orientations: application to focal mechanism data of recent British earthquakes. Geophys. J. Int. 110, 276–282.

Lisle, R.J., 1998. Simple graphical constructions for the direction of shear. J. Struct. Geol. 20, 969–973.

Lisle, R.J., 2013. A critical look at the Wallace-Bott hypothesis in fault-slip analysis. Bull. la Soc. Geol. Fr. 184, 299–306. https://doi.org/10.2113/gssgfbull.184.4-5.299.

Maerten, L., 2000. Variation in slip on intersecting normal faults: Implications for paleostress inversion. J. Geophys. Res. Solid Earth 105, 25553–25565. https://doi.org/10.1029/2000JB900264.

Maerten, F., Madden, E.H., Pollard, D.D., Maerten, L., 2016. Incorporating fault mechanics into inversions of aftershock data for the regional remote stress, with application to the 1992 Landers, California earthquake. Tectonophysics 674, 52–64.

Maerten, L., Maerten, F., Lejri, M., 2018. Along fault friction and fluid pressure effects on the spatial distribution of fault-related fractures. J. Struct. Geol. 108, 198–212.

Marrett, R., Allmendinger, R.W., 1990. Kinematic analysis of fault-slip data. J. Struct. Geol. 12, 973–986.

Martin, C.D., Lanyon, G.W., 2003. Measurement of in-situ stress in weak rocks at Mont Terri Rock Laboratory, Switzerland. Int. J. Rock Mech. Min. Sci. 40, 1077–1088.

Martínez-Garzón, P., Kwiatek, G., Bohnhoff, M., Dresen, G., 2016. Impact of fluid injection on fracture reactivation at The Geysers geothermal field. J. Geophys. Res. Solid Earth 121, 7432–7449. https://doi.org/10.1002/2016JB013137.

Mattauer, M., Mercier, J.L., 1980. Microtectonique et grande tectonique. Mémoires hors série la Soc. géologique Fr. 10, 141–161.

McGarr, A., 2014. Journal of Geophysical Research: Solid Earth. J. Geophys. Res. Solid Earth 1–12. https://doi.org/10.1002/2013JB010597.Received.

Meng, C., Heltsley, W., Pollard, D.D., 2012. Evaluation of the Eshelby solution for the ellipsoidal inclusion and heterogeneity. Comput. Geosci. 40, 40–48. https://doi.org/10.1016/j.cageo.2011.07.008.

Mercier, J.L., Sorel, D., Vergely, P., Simeakis, K., 1989. Extensional tectonic regimes in the Aegean basins during the Cenozoic. Basin Res. 2, 49–71.

Mura, T., 1987. Micromechanics of Defects in Solids, 2nd revised edn. Mechanics of Elastic and Inelastic Solids. Martinus Nijhoff, Dordrecht.

Nieto-Samaniego, Á., Alaniz-Alvarez, S., 1997. Origin and tectonic interpretation of multiple fault patterns. Tectonophysics 270, 197–206. https://doi.org/10.1016/S0040-1951(96)00216-8.

Nussbaum, C., Bossart, P., Amann, F., Aubourg, C., 2011. Analysis of tectonic structures and excavation induced fractures in the Opalinus Clay, Mont Terri underground rock laboratory (Switzerland). Swiss J. Geosci. 104, 187–210. https://doi.org/10.1007/s00015-011-0070-4.

Pascal, C., 2002. Interaction of faults and perturbation of slip: Influence of anisotropic stress states in the presence of fault friction and comparison between Wallace-Bott and 3D distinct element models. Tectonophysics 356, 307–322. https://doi.org/10.1016/S0040-1951(02)00413-4.

Petit, J.P., 1987. Criteria for the sense of movement on fault surfaces in brittle rocks. J. Struct. Geol. 9, 597–608. https://doi.org/10.1016/0191-8141(87)90145-3.

Pollard, D.D., Segall, P., 1987. Theoretical displacements and stresses near fractures in rock. Fracture Mechanics of Rock. BK Atkinson 277–349.

Pollard, D.D., Saltzer, S.D., Rubin, A.M., 1993. Stress inversion methods: are they based on faulty assumptions? J. Struct. Geol. 15, 1045–1054. https://doi.org/10.1016/0191-8141(93)90176-B.

Reches, Z., 1987. Determination of the tectonic stress tensor from slip along faults that obey the Coulomb yield condition. Tectonics 6, 849–861.

Roche, V., van Der Baan, M., Preisig, G., 2018. A study of 3D modeling of hydraulic fracturing and stress perturbations during fluid injection. J. Pet. Sci. Eng. 170, 829–843. https://doi.org/10.1016/j.petrol.2018.06.037.

Shapiro, S.A., Dinske, C., 2009. Fluid-induced seismicity: pressure diffusion and hydraulic fracturing. Geophys. Prospect. 57, 301–310. https://doi.org/10.1111/j.1365-2478.2008.00770.x.

Shapiro, S.A., Audigane, P., Royer, J.J., 1999. Large-scale in situ permeability tensor of rocks from induced microseismicity. Geophys. J. Int. 137, 207–213. https://doi.org/10.1046/j.1365-246X.1999.00781.x.

Shapiro, S.A., Patzig, R., Rothert, E., Rindschwentner, J., 2003. Triggering of seismicity by pore-pressure perturbations: permeability-related signatures of the phenomenon. In: Thermo-Hydro-Mechanical Coupling in Fractured Rock. Springer, pp. 1051–1066.

Soliva, R., Maerten, F., Petit, J.-P., Auzias, V., 2010. Field evidences for the role of static friction on fracture orientation in extensional relays along strike-slip faults: comparison with photoelasticity and 3-D numerical modeling. J. Struct. Geol. 32, 1721–1731.

Terakawa, T., Miller, S.A., Deichmann, N., 2012. High fluid pressure and triggered earthquakes in the enhanced geothermal system in Basel, Switzerland. J. Geophys. Res. Solid Earth 117, 1–15. https://doi.org/10.1029/2011JB008980.

Twiss, R.J., Gefell, M.J., 1990. Curved slickenfibers: a new brittle shear sense indicator with application to a sheared serpentinite. J. Struct. Geol. 12, 471–481. https://doi.org/10.1016/0191-8141(90)90035-W.

Vandycke, S., Bergerat, F., Dupuis, C., 1991. Meso-cenozoic faulting and inferred palaeostresses in the Mons Basin, Belgium. Tectonophysics 192, 261–271. https://doi.org/10.1016/0040-1951(91)90103-Y.

Wallace, R.E., 1951. Geometry of shearing stress and relation to faulting. J. Geol. 59, 118–130. https://doi.org/10.1086/625831.

Wallace, R.E., Morris, H.T., 1986. Characteristics of faults and shear zones in deep mines. Pure Appl. Geophys. 124, 107–125.

Walsh, J.B., 1981. Effect of pore pressure and confining pressure on fracture permeability, in: International Journal of Rock Mechanics and Mining Sciences & Geomechanics Abstracts. Elsevier, pp. 429–435.

Wibberley, C.A.J., Shipton, Z.K., 2010. Fault zones: a complex issue. J. Struct. Geol. 32 (11), 1554–1556.

Witherspoon, P.A., Wang, J.S.Y., Iwai, K., Gale, J.E., 1980. Validity of cubic law for fluid flow in a deformable rock fracture. Water Resour. Res. 16, 1016–1024.

Yamaji, A., 2000. The multiple inverse method: a new technique to separate stresses from heterogeneous fault-slip data. J. Struct. Geol. 22, 441–452. https://doi.org/10.1016/S0191-8141(99)00163-7.

Zoback, M.D., Harjes, H.-P., 1997. Injection-induced earthquakes and crustal stress at 9 km depth at the KTB deep drilling site, Germany. J. Geophys. Res. Solid Earth 102, 18477–18491. https://doi.org/10.1029/96JB02814.

Zoback, M.L., Anderson, R.E., Thompson, G.A., 1981. Cainozoic evolution of the state of stress and style of tectonism of the Basin and Range province of the western United States. Philos. Trans. R. Soc. A Math. Phys. Eng. Sci. 300, 407–434. https://doi.org/10.1098/rsta.1981.0073.